A Multiphysics Simulation Approach for Efficient Modeling of Lightning Strike Tests on Aircraft Structures

A Multiphysics Simulation Approach for Efficient Modelling of a Waveform-B Lightning Strike Test

Gasser F. Abdelal [1], Adrian Murphy [2]

[1, 2] *School of Mechanical and Aerospace Engineering, Queen's University, Belfast, UK.*

[1] *g.abdelal@qub.ac.uk, phone: +44 (0)28 9097 4123, Fax: +44 (0)28 9097 4148*

Abstract

A numerical approach is proposed and demonstrated for efficient modelling of the thermal plasma behaviour present during a lightning strike event. The approach focuses on events with time-scales from microseconds to milliseconds and combines the finite element method, Magnetohydrodynamics and Similitude theory. Similitude theory is used to scale the problem to require considerably less computing resource. To further reduce the computational burden and to resolve the numerical difficulty of simulating the nearly zero electrical conductivity of air at room temperature an approach based on cold field electron emissions is introduced. Simulations considering turbulent flow have been considered, modelling a test configuration from literature designed to inspect composite material performance and applying an aerospace standard test profile (waveform-B). Predicted peak temperatures (of the order of ~40,000 K) and pressures (of the order of 0.1-0.2 MPa) suggest that the pressure loading during a waveform-B event will have a minimal effect on composite material damage.

Introduction

Modelling thermal plasma due to a lightning strike will allow the estimation of electric current density, plasma pressure, and heat flux at the surface of the aircraft. Such understanding of the behaviour at the aircraft surface would enable better estimation of the mechanical and thermal induced loading on the structure and the prediction of structural damage. Such understanding of the loading and damage mechanics could ultimately lead to the design of better lightning protection systems [1].

A lightning strike on a structure generates thermal plasma with a time-scale of microseconds to milliseconds. Simulating a thermal plasma with a time-scale of seconds, for example laser welding or plasma-cutting processes, has previously been achieved using Magnetohydrodynamics modelling [2]. However, the considerable reduced time-scale and greater energy involved in a lightning event requires a considerably larger number of discretised elements and iteration steps to converge to a solution and this makes such analysis incredibly challenging.

A lightning channel is a thermal plasma (temperature > 10,000 c^o) that consists of electrons, atoms and molecules at a ground or excited state, positive ions, negative ions and photons. Accurate simulation of a thermal plasma requires calculating the plasma composition and estimation of thermodynamic and transport properties [3]. COMSOL Multiphysics [4] has a module that models thermal plasma, which can represent atomic and molecular theory, and

gaseous electronics. Simulating the lightning channel thermal plasma is a requirement to predict the electric current density profile, pressure wave profile, heat flux profile applied on the aircraft structure.

In order to demonstrate an aircraft can withstand a range of lightning strike events during service a mature set of test standards and regulations are in place. Central to these standards and regulations is the definition of four test Waveforms (Waveform-A to -D) for evaluating direct effects (i.e. damage to the structure) Fig. 1 [5]. Waveform A represents the first return stroke, current Waveform-B and -C represent the lightning environment that might be caused by the intermediate and long duration currents following some return strokes or re-strikes, and current Waveform-D represents a subsequent stroke. It can be seen from Fig. 1, which is not to scale, that Waveform-B and -C show much lower peak amplitudes than Waveform-A and -D, but represent very high charge transfer. Waveform-B and -C can be thought as currents that act as a bridge between the initial stroke Waveform-A and a subsequent stroke, Waveform-D.

To date a number of researchers have created numerical simulations of lightning strike Waveform-C, which is of a time scale in the range of seconds [6]. However expanding these models to simulate Waveform-B or D is not trivial due to the hardware resources required. Preceding work has suggested 70 days on a HPC Windows cluster [7] to complete a full-scale model. Thus, novel approaches are required to idealise and simulate testing with the shortest duration Waveforms.

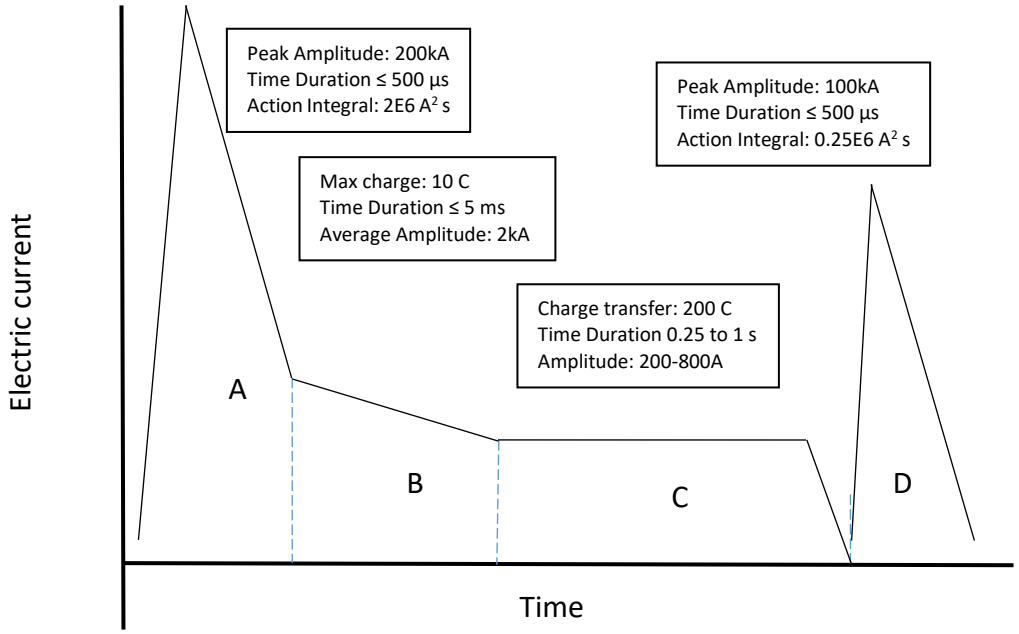

Figure 1: Typical simulated lightning current waveforms [5].

Thermal plasma generated during laser cutting, electric (laser) welding and other plasma processing techniques has been the focus of research for a number of decades. For engineering applications the plasma is typically modelled using Magnetohydrodynamics

(MHD), a technique that predicts gross plasma behaviour rather than the behaviour of the individual plasma components (i.e. electrons, atoms, etc.). MHD [8-18] studies the motion of an electrically conducting fluid in the presence of an applied magnetic field. Once the fluid starts conducting electricity, a magnetic field is induced and this applies electromagnetic forces on the flow. The magnetic force (Lornetz force) modifies the fluid flow velocity and pressure profiles. Thus the governing equations of MHD describe the motion of a conducting fluid in a magnetic field and are a combination of the Maxwell's equations of electromagnetism, the Navier–Stokes equations of fluid and the thermal conductivity heat transfer equations. These partial differential equations can be solved numerically using the finite element method or the finite volume method. For both methods commercial software which will be familiar to the engineering community is available (e.g. COMSOL, Fluent).

Herein the lightning strike electric arc model is based on the preceding Gas Tungsten Arc (GTA) models available in the literature [19–29]. In general the preceding plasma modelling has assumed the thermal plasma to be in local thermodynamic equilibrium. These models thus assume that the plasma electrons and the heavy species have equal temperature. Different numerical techniques have been developed to couple the Navier Stokes, Heat transfer and Electromagnetic equations assuming the thermal plasma is a single laminar gas flow.

Considering the previous research a number of these works have simulated the arc-plasma region with imposed temperature values at the cathode and anode boundaries [19–21]. Others have attempted to model the temperature generating physics between the anode and cathode. These models take into account the discontinuity phenomena between the anode and the arc-plasma interface. The Lago and Gonzalez et al. models [22, 23] did not include the cathode region in their simulations, but developed a model to simulate the effect of metal vapour in the plasma column combined to a moving welding torch. The plasma models of Tanaka and Lowke summarized in [25, 26] are the most complete, based on the Sansonnens et al. model [27], they also include the cathode and anode regions with weld pool formation, and the boundary conditions are directly applied at the external borders with no assumption on the cathode surface temperature.

Traidia [30] perform coupled simulation between the welding arc and the weld pool dynamics for a pulsed gas tungsten arc welding process. Tanka proposed using thermal field emission and a temperature boundary condition (3,500 K) at the cathode to simulate the air electric conductivity at room temperature. In this case the simulation only considered the plasma welding in a steady state condition. In such a case the boundary condition would heat up the adjacent air, increasing the air electric conductivity. Traidia developed the Tanaka model to simulate a transient plasma welding process, however in this case the same technique was not applied to resolve the problem of zero electric conductivity at room temperature. Traidia removed the 3,500 K boundary condition at the cathode, replacing it with a 1 mm high electric conducting layer towards the plasma region. In this case the introduced layer had equivalent electric conductivity properties to that of the cathode material. However, the electron transport equations were excluded from the simulation and it is not clear from the paper if this was due to a longer simulation time, once electron drift-diffusion equations were included in the model or there were no thermal field emissions at room temperature.

Methodology

Clearly, there is a computational challenge associated with air electric conductivity at room temperature. In order to progress this topic a broader review of the literature has been undertaken and this has identified a number of significant works. Kamsali et al. [31] conducted air electric conductivity measurements in atmosphere at room temperature and reported it to be approximately 1E-14 S/m. Additionally, electron cold field emissions based on Fowler and Nordheim's work [32] has the potential to model the critical behaviour, which is discussed also in Forbes et al. [33]. Equation 1 presents the relationship between electron emission and electric field properties

$$J_{FN} = A_{fn}\, normE^2 \exp\left(-\mathrm{B}_{fn}\frac{\phi_c^{1.5}}{normE}\right) \tag{1}$$

Where ϕ_c is cathode material work function, A_{fn} (1.541434e-6A eV V^{-2}/ϕ_c) is the first Fowler-Nordheim constant, B_{fn} (6.83089 $eV^{-1.5}$ V nm^{-1}) is the second Fowler-Nordheim constant, and normE is the electric field at the emitter surface. Thus modelling cold electron field emissions is proposed herein as the solution to the computational challenge associated with the low electric conductivity of air at room temperature. The motivation behind assuming cold field emissions is during preliminary simulations the electric field reached a value higher than 1E+7 V/m in the vicinity of the cathode. However, the electron flux was not high enough to increase the electric conductivity. The other factor is the high electric field, which accelerates the ionization process of the air using the emitted electrons. This process would increase the electric conductivity considerably, opening a channel for the lightning strike electric current to reach the anode surface.

However, to fully couple the electron transport equations with the Magnetohydrodynamics model resulted in a dramatic slowing of simulation progress - with simulation times of the order of 3 days to progress a very basic, highly idealised model a few microseconds. Therefore, an approach to represent the electron transport equations using a 1-D model was created, which would run for an initial period (of the order of 4e-5 seconds) to represent the initial electron emissions, ionization, and attachment of the connecting channel between the cathode and anode. The rationale for only simulating the electron transport for a short time period using the 1-D model is that once the electric conductivity increases, the electric field value drops considerably, which eliminates the electron field emissions and the main source of the electron ionization process becomes the air electric resistivity.

Having addressed the major challenge associated with the initiation of the lightning arc the challenge then for a usable simulation is the stability criteria of the heat transfer analysis. This requires the satisfaction of Equation 2,

$$\Delta t \;>\; \frac{\rho\, c_p}{6\,k}\,\Delta l^2 \tag{2}$$

Where Δt is the transient heat transfer time increment, ρ is the material density, c_p is the material specific heat, k is the material thermal conductivity, and $\Delta \ell$ is a typical finite element mesh dimension. The smaller the time-step required for convergence, the smaller the finite element mesh characteristic length. Thus simulating the thermal plasma due to Waveforms-

A, -D, which are of a microseconds scale or waveform B, which is of a milliseconds scale requires an impractical number of model elements. Again, considering preliminary simulations a Waveform-B analysis suggested time-steps of the order of 1E-10 seconds and HPC run times of greater than 50 days.

This paper proposes a solution to the above problem by applying the similitude theory [34] to create virtual prototype models of equivalent physics. Such virtual prototype models will have a significant reduced computational cost but have the potential to represent the critical behaviour present in a strike event. This paper will thus be the first in simulating the lighting strike of Waveform-B (milliseconds time scale) and with the realistic potential to simulate Waveforms-A and -D (Fig. 1).

Similitude is a mathematical science that includes similarity and dimensional analysis. Similarity means that two physical systems are similar if special non-dimensional ratios are equal in both systems [35]. The requirements of similitude are derived from the main partial differential equations, initial conditions and the boundary conditions that describe the system. The first step is to derive the non-dimensional form of the main equations that model the systems. This derivation will produce non-dimensional terms, which are called similarity conditions. The first constraint of the similitude is the equality of these similarity conditions in both the prototype and the full-scale model. The second similarity constraint is the equality of the non-dimensional independent variables, which constitute the non-dimensional initial, and boundary conditions [30]. The input to the thermal plasma simulations is the waveform electric current profile, and the electromagnetic field is the main volume force that drives the flow in the fluid domain, which makes the electromagnetic model the driving force in the simulation. Initially, an absolute model of the electromagnetic system must be derived that relates the independent variables in both the full scale and the prototype models, before deriving the similarity conditions of the MHD system.

Model formulation

The following sections outline the assumptions and basic equations, which describe the electric, magnetic, fluid flow, heat transfer and Electron transport behaviour to be modelled. Two major overarching assumptions are made:

- The plasma is at local thermodynamic equilibrium (LTE), which assumes electron temperature is equivalent to the heavy species temperature.
- The fluid flow is Newtonian and either laminar or turbulent.

Electric Module (ec) & Magnetic Module (mf)

The electromagnetic behaviour is modelled using Maxwell's equations under the variable waveform electric current, Equations 3 to 8,

$$\nabla \times H = \sigma E + \varepsilon \frac{\partial E}{\partial t} \tag{3}$$

$$\nabla \times E = -\mu \frac{\partial H}{\partial t} \tag{4}$$

$$B = \mu H, \quad D = \varepsilon E \tag{5}$$

$$E = -\nabla V - \frac{\partial A}{\partial t} \tag{6}$$

$$J = \sigma\left(E + u \times B\right) + \frac{\partial D}{\partial t} \tag{7}$$

$$\sigma \frac{\partial A}{\partial t} + \nabla \times \left(\frac{1}{\mu} \nabla \times A \right) + \sigma \nabla V = 0 \tag{8}$$

Where, H is the vector magnetic field intensity, D is the electric displacement vector, σ is the electrical conductivity of the corresponding domain (cathode, plasma, anode), J is the current density, ε is the dielectric constant (permittivity), μ is the domain permeability, E is the electrical field intensity, V is the electrical potential, B is the magnetic flux density, and A is the magnetic potential.

Fluid Flow Equations (spf)

The fluid flow is modelled applying the turbulent flow equations, Equations 9 to 12,

$$\frac{\partial \rho}{\partial t} + \nabla \bullet \left(\rho u\right) = 0 \tag{9}$$

$$\rho\left(\frac{\partial u}{\partial t} + u \bullet \nabla u \right) = \nabla \bullet \left[-p\mathrm{I} + (\mu + \mu_T)\left(\nabla u + \left(\nabla u\right)^T \right) - \frac{2}{3}\mu\left(\nabla \bullet u\right)\mathrm{I} \right] + J \times B \tag{10}$$

$$\begin{aligned} \frac{\partial\left(\rho k\right)}{\partial t} + \rho\left(u \bullet \nabla\right)k &= \nabla \bullet \left[\left(\mu + \frac{\mu_T}{\sigma_k} \right) \nabla k \right] - \rho\varepsilon + \mu_T P_k \\ \frac{\partial\left(\rho \varepsilon\right)}{\partial t} + \rho\left(u \bullet \nabla\right)\varepsilon &= \nabla \bullet \left[\left(\mu + \frac{\mu_T}{\sigma_\varepsilon} \right) \nabla k \right] - \rho C_2 \frac{\varepsilon^2}{k} + \mu_T C_1 \frac{\varepsilon}{k} P_k \end{aligned} \tag{11}$$

$$\begin{aligned} \mu_T &= \rho C_\mu \frac{k^2}{\varepsilon} \\ P_k &= \mu_T \left[\nabla u : \left(\nabla u + \left(\nabla u\right)^T \right) \right] \end{aligned} \tag{12}$$

Where, the k-ε turbulent model is used. The turbulent model adds two additional transport equations and two dependent variables to the Navier-Stokes equations. The turbulent kinetic energy, k, and the turbulent dissipation rate, ε. u is the velocity vector field, t is time, ρ is density, μ is viscosity, p is the pressure field, J is electric current density, B is the magnetic flux density, μ_T is the turbulent viscosity, P_k is the production term, and (C_1, C_2, C_μ) are turbulence model parameters. It is worth noting at this point that the choice of the turbulence model parameters is very important for simulation convergence and the accuracy of any flow predictions.

Heat Transfer Module (ht)

The energy conservation equation is used to model heat transfer in the fluid and solid domains, Equations 13,

$$\rho\, C_p \left(\frac{\partial T}{\partial t} + \vec{\upsilon} \bullet \nabla T \right) = \nabla \bullet \left(k \nabla T \right) + \vec{J} \bullet \vec{E} + \frac{5\, k_B}{2\, e} \vec{J} \bullet \nabla T - 4\pi \varepsilon_N \quad (13)$$

The last three terms in the above equations are; the joule heating, the electronic enthalpic flux, and the plasma radiation loss respectively. Where T is the temperature, k is the thermal conductivity, K_B is the Boltzmann constant, e is the electron charge, and ε_N is the net emission coefficient of plasma [30]. Traidia [30] recommended modelling a sheath thin layer of thickness 1 x 10^{-4} m next to the anode surface to simulate the NLTE (no thermodynamic thermal equilibrium) condition for the heavy species temperature in this layer as it differs from the electron temperature. This transition sheath zone is modelled as an ohmic conductor, which ensures the transition between plasma and the cathode. Within this layer, the electric conductivity corresponds to the cathode, while the other material properties correspond to the plasma. In addition, the ohmic sheath zone permeability is very low (~1e-15). The heat flux at the boundary between the anode and the plasma has to satisfy the Equation 14 [30],

$$\vec{q}_{anode} \bullet \vec{n} - \vec{q} \bullet \vec{n} = \left| \vec{J} \bullet \vec{n} \right| \phi_a - \varepsilon\, k_B\, T^4 \quad (14)$$

Where, n is the normal vector to the top surface, ϕ_a is the work function of the anode, e is the anode emissivity and k_B the Boltzmann's constant. The first term $\left| \vec{J} \bullet \vec{n} \right| \phi_a$ represents the heating by electron condensation (energy received by the anode from the incoming electrons). The second term $\varepsilon\, k_B\, T^4$ represents the radiation cooling losses. The heat flux at the boundary between the cathode and the plasma has to satisfy the Equation 15 [26],

$$\vec{q}_{cathode} \bullet \vec{n} - \vec{q} \bullet \vec{n} = j_i\, V_i - j_e\, \phi_c - \varepsilon\, k_B\, T^4 \quad (15)$$

Where, j_i and j_e are respectively the ion current and the electron current, φ_c is the cathode work function, and V_i is the air ionization potential. The first term $j_i\, V_i$ represents the heating energy received by the cathode from the impacted ions. The second term $j_e\, \phi$ represents the energy consumed at the cathode to emit electrons. The electron and ion currents are calculated from Equation 16 [30],

$$\begin{aligned} j_r &= A_r T^2 \exp\left(\frac{-e\, \phi_e}{\sigma_B\, T} \right) \\ j_e &= \begin{cases} j_r & if \left(\left| \vec{J} \bullet \vec{n} \right| - j_r \right) > 0 \\ \left| \vec{J} \bullet \vec{n} \right| & if \left(\left| \vec{J} \bullet \vec{n} \right| - j_r \right) \le 0 \end{cases} \\ j_i &= \left| \vec{J} \bullet \vec{n} \right| - j_e \end{aligned} \quad (16)$$

Where, A_r is the Richardson's constant, ϕ_e the effective work function for thermionic emission and the elementary charge.

Electron Transport Equations

The main objective of modelling the electron transport is to calculate the initial extra electric conductivity due to the electron cold-field emission and ionization. Electron transport is modelled applying the time-dependent PDE Equation 17,

$$\begin{aligned} &\frac{\partial n_e}{\partial t} + \nabla\cdot\left(-D_e\,\nabla n_e\right) + W_e\cdot\nabla n_e = R_i \\ &\Gamma_e = -D_e \nabla n_e + W_e n_e \\ &W_e = \left(\mu_{er} / N_n\right) E \\ &R_i = \left(n_e \alpha_{er} W_e\right) - \left(n_e \eta_{er} W_e\right) \end{aligned} \tag{17}$$

Where, n_e is the electron density [1/m^3], D_e is the electron diffusion coefficient, W_e is the electrons average velocity, N_n is the gas density [1/m3], μ_{er} is the electrons reduced mobility [1/(mVs)], α_{er} is the electrons reduced ionization coefficient [m^2], η_{er} is the electrons reduced attached coefficient [m^2], Γ_e is the electrons flux [1/(m^{2}s)], and R_i is the electrons source term [1/(m^{3}s)]. The electron transport coefficients are defined in [30]. The electron flux is defined at the cathode using Equation 18,

$$-n \bullet \Gamma_e = \left(\frac{J_{FN}}{e_{const}}\right) \quad [1/m^2 s] \tag{18}$$

Where, J_{FN} is the electron cold field emission flux and e_{const} is electron elementary charge. The plasma extra electric conductivity due to electron cold-field emissions and ionization, is defined in Equation 18 as,

$$\sigma_e = n_e e_{const} \mu_{er} / N_n \quad [S/m] \tag{19}$$

Similitude Modelling Equations

George [34] discussed two types of electromagnetic models; a geometrical model and an absolute model. The geometrical model simulates the geometrical configuration, while ignoring the power level of the full-scale system. The absolute model simulates both the geometrical configuration and the power level of the full-scale system. However, George [34] in his earlier attempt to derive both models based on Maxwell's equations, stressed that the derivation is valid if the Maxwell's equations are linear. Nonlinearity of Maxwell's equations comes from modelling nonlinear media where ε permittivity is a function of E electric field intensity. The Maxwell's equations used in modelling thermal plasma are assumed linear and ε permittivity equals that of air. For an absolute electromagnetic model, the conditions in Equation 20 are applied,

$$\begin{aligned} &(x, y, z) = d\ (x', y', z') \\ &t = \gamma\ t' \\ &E\left(x, y, z\right) = \alpha\ \mathrm{E}'\left(x', y', z', t'\right) \\ &H\left(x, y, z\right) = \beta\ H'\left(x', y', z', t'\right) \end{aligned} \tag{20}$$

where *d* is the scale factor for space, *ϒ* is the scale factor for time, *α* is the scale factor for electric field intensity, and *β* is the scale factor for magnetic field intensity. Primed variables refer to the absolute model, while unprimed variables refer to the full-scale model. Once the four scale parameters are estimated, Maxwell's equations can be used to derive the relationship between other electromagnetic quantities (*I, V, B, ε, μ*, etc.) in both systems. Rewriting Equation 13 for the absolute model and substituting in Equations 1 and 2 results in Equation 21,

$$\begin{aligned}\frac{d}{\beta}\nabla\times H\left(x,y,z,t\right)&=\sigma'\left(x',y',z',t'\right)\frac{E\left(x,y,z,t\right)}{\alpha}+\frac{\gamma}{\alpha}\varepsilon'\left(x',y',z',t'\right)\frac{\partial E\left(x,y,z,t\right)}{\partial t}\\ \frac{d}{\alpha}\nabla\times E\left(x,y,z,t\right)&=-\frac{\gamma}{\beta}\mu'\left(x',y',z',t'\right)\frac{\partial H\left(x,y,z,t\right)}{\partial t}\end{aligned}\tag{21}$$

The similarity between Equations 13 and 14 is to satisfy the following constraints, Equation 22,

$$\begin{aligned}\sigma'&=\frac{d\alpha}{\beta}\sigma\\ \varepsilon'&=\frac{d\alpha}{\beta\gamma}\varepsilon\\ \mu'&=\frac{d\beta}{\alpha\gamma}\mu\end{aligned}\tag{22}$$

The current density vector J' and magnetic flux density of the absolute model, Equation 23,

$$\begin{aligned}J'&=\sigma'E'=\frac{d\alpha\sigma}{\beta}\frac{E}{\alpha}=\frac{d}{\beta}J\\ B'&=\mu'H'=\frac{d\beta}{\alpha\gamma}\mu\frac{B}{\mu}\frac{1}{\beta}=\frac{d}{\alpha\gamma}B\end{aligned}\tag{23}$$

The total current in I' and voltage V' of the absolute model, Equation 24,

$$\begin{aligned}I'&=\int_{a'}J'\bullet n'\,da'=\int_{a}d\frac{J}{\beta}\bullet n\frac{da}{d^2}=\frac{I}{d\beta}\\ V'&=\int_{P1'}^{P2'}E'\bullet dl'=\int_{P1}^{P2}\frac{E}{\alpha}\bullet\frac{dl}{d}=\frac{V}{\alpha d}\end{aligned}\tag{24}$$

where *n, n'* are perpendicular vectors on areas *a, a'* respectively, *dl* is a vector element of length along a curve between two points *P1, P2*.

To this point an absolute model of the electromagnetic system is derived as a function of four scale parameters. These parameters are *d* for space, *ϒ* for time, α for electric field and β for magnetic field. The electromagnetic system was chosen as the main scale point for the rest of the MHD equations due to the fact that the electric current and magnetic field are the input and driving force of the lightning strike simulation. Next, the similitude theory can be applied on the MHD equations to derive the similarity constraints that are required to develop a

virtual prototype model with simpler characteristics and computationally less burdensome to simulate.

Based on the work of Kalikhman [35] and Victor [36], non-dimensional MHD was derived, Equation 25,

$$\begin{aligned}
&\tilde{\rho}\frac{\partial \tilde{u}}{\partial \tilde{t}}\bullet\frac{L}{u_0 t_0}+\tilde{\rho}\left(\tilde{u}\frac{\partial \tilde{u}}{\partial \tilde{x}}+\tilde{v}\frac{\partial \tilde{u}}{\partial \tilde{y}}\right)=-\frac{\partial \tilde{p}}{\partial \tilde{x}}\bullet\frac{p_0}{\rho_0 u_0^2}+\ldots\\
&\frac{\partial}{\partial \tilde{x}}\left[\tilde{\eta}\left(\frac{4}{3}\frac{\partial \tilde{u}}{\partial \tilde{x}}-\frac{2}{3}\frac{\partial \tilde{v}}{\partial \tilde{y}}\right)\right]\frac{\eta_0}{u_0 L\rho_0}+\frac{\partial}{\partial \tilde{y}}\left[\tilde{\eta}\left(\frac{\partial \tilde{u}}{\partial \tilde{y}}+\frac{\partial \tilde{v}}{\partial \tilde{x}}\right)\right]\frac{\eta_0}{u_0 L\rho_0}+\ldots\\
&\left(\tilde{J}_y\tilde{B}_z-\tilde{J}_z\tilde{B}_y\right)\frac{J_0 B_0 L}{\rho_0 u_0^2}
\end{aligned} \tag{25}$$

$$\begin{aligned}
&\tilde{\rho}\tilde{c}_p\frac{\partial \tilde{T}}{\partial \tilde{t}}=\frac{k_0 t_0}{\rho_0 c_{p0} L}\frac{\partial}{\partial \tilde{x}_i}\left(\tilde{k}_{ij}\frac{\partial \tilde{T}}{\partial \tilde{x}_j}\right)+\frac{q_{g0}t_0}{\rho_0 c_{p0}T_0}\tilde{q}+\ldots\\
&\frac{J_0 k_B T_0}{e\rho_0 u_0 c_{p0}T_0}\left(\frac{5}{2}\frac{k_B}{e}\tilde{\tilde{J}}\bullet\nabla\tilde{T}+\tilde{\rho}c_p\tilde{\tilde{u}}\bullet\nabla\tilde{T}\right)
\end{aligned} \tag{26}$$

Where q_g is the rate of the heat generated per unit volume, variables with zero subscript are reference parameters. Based on the non-dimensional analysis of the MHD the similitude constraints may then be derived. Each of the similitude constraints are then used with the Equations 15 to 17 to derive the relationships for the fluid flow and heat variables in the prototype and the full scale equations, Equation 27,

$$\begin{aligned}
&\frac{L}{\tau u}\Rightarrow u_m=\frac{\gamma}{d}u_F,\quad \frac{\sigma B^2 L}{\rho u}\Rightarrow \rho_m=\frac{d^3}{\beta\alpha\gamma^3}\rho_F,\quad \frac{uL\rho}{\eta}\Rightarrow\eta=\frac{d}{\beta\alpha\gamma^2}\eta\\
&\frac{JT}{\rho u c_p T}\Rightarrow c_{pm}=\frac{\alpha\gamma^2}{d}c_{pF},\quad \frac{u\eta}{L\rho c_p T}\Rightarrow T_m=\frac{1}{d\alpha}T_F\\
&\frac{\eta c_p}{k}\Rightarrow k_m=\frac{1}{\beta}k_F,\quad \frac{\varepsilon_N\tau}{\rho c_p T}\Rightarrow\varepsilon_{Nm}=\frac{d}{\beta\alpha}\varepsilon_{NF}
\end{aligned} \tag{27}$$

where *m* refers to the virtual prototype model, *F* refers to the full-scale model, and the characteristic values for *u, ρ, μ, σ, η, C_p, K, T_F, ε_N* are chosen at randomly selected coordinates (x_0, y_0, z_0). Thus, a prototype model can be developed in two steps; initially, calculation of the electromagnetic absolute model material properties (*ε, μ, σ*) based on the scaled input electric current *I* and the four scaling parameters (*α, β, Υ, d*), may then be used as similitude constraints to calculate the fluid flow and the heat flow modules' scaled material properties (i.e. ρ, η, C_p, k). The objective of scaling is to slow down the applied Waveform lighting strike electric current, thus allowing the numerical simulations to use larger time increments without violating the heat transfer constraint, Equation 2.

Waveform-B Simulation

COMSOL Multiphysics is used to model the MHD Equations 3 to 16 to simulate the thermal plasma due to lighting strike Waveform-B as defined in the SAE ARP 5412 [5]. The lightning strike experimental configuration simulated is similar to the one used by Hirano et al. [37],

Ogasawara et al. [38], and Feraboli & Miller [39] to inspect composite material performance. The calculation domain and boundary conditions are shown in Figure 2 and Table 3. The model consists of three basic domains, cathode, anode and fluid (air plasma). The anode in this simulation is the aircraft structure. Air plasma's transport properties are taken from references [31, 40]. Capitelli et al. [40] calculated air transport properties in the temperature range 50-100,000 K applying the perturbative Chapman-Enskog method, while assuming the air plasma is in local thermodynamic equilibrium (LTE). However as noted in the methodology the air initial electric conductivity is calculated using a 1-D model that couples the electric field and electron transport partial differential equations. The 1-D model is discussed in the next section. Material properties for the anode and the cathode domains are defined as a function of temperature (COMSOL Material Library). Zero initial conditions are assumed for all domains. Table 2 defines the material properties for all domains.

Using scaling factors, the relationship between the input scaled and original electric current Waveform-B is given in Equation 28,

$$I'(t) = \frac{11300}{d\ \beta}\left(e^{-700\bullet t'\bullet\gamma} - e^{-2000\bullet t'\bullet\gamma}\right) = 113\left(e^{-70\bullet t'} - e^{-200\bullet t'}\right) \tag{28}$$

The model was then used to calculate the electromagnetic, fluid flow, and heat transfer scaled material properties based on the absolute model and similitude constraint Equations 22, 23, and 27. Based on a number of trial simulation conditions a set of similitude parameters where converged upon (ϒ=1e-4, α=1e8, β=1e8, d=2). A mesh convergence study defined a mesh of 71,353 elements, Figure 2.

Table 2. Material properties vs. temperature of full-scale model.

Air Gas Thermal Plasma Properties. Air ionization potential = 12.1 V.						
Temp., K	σ, S/m	C_P, J/Kg/K	K, W/m/K	ρ, Kg/m^3	η, Kg/m/s	ε_N, W/m^3
300	1e-14	1.0473e3	4.137e-2	0.70208	2.705e-5	0
5000	0.2273e2	2.7245e3	7.105e-1	5.838e-2	1.496e-4	1e5
7000	0.3277e3	1.4026e4	4.0697	2.723e-2	1.951e-4	1e6
10000	3264	4.8672e3	1.7086	1.72e-2	2.453e-4	1e7
15000	8418	2.1652e4	5.3685	7.748e-3	1.188e-4	1e9
20000	11680	6.1585e3	3.3881	4.548e-3	4.292e-5	3e9
24000	13379	1.099e4	4.2831	3.619e-3	4.292e-5	5e9
Cathode: Tungsten [solid, Ho et al]. COMSOL Material Library. Cathode work function = 4.52 V, effective work function = 2.63 V [30]. Anode: Copper. COMSOL Material Library.						

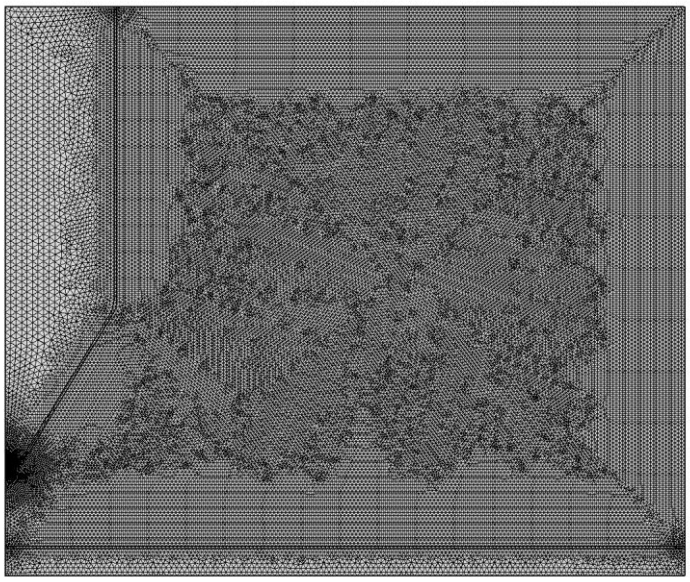

Figure 2: Simulation axisymmetric mesh.

Table 3: Axisymmetric model boundary conditions.

	ab	bc	cd	de	ef	dg	fg	gh	hb
Electrical current	-n . J = J_n	n . J = 0	n . J = 0	n . J = 0	V = 0		Axial symmetry	Axial symmetry	
Magnetic field	n x A = 0	n x A = 0	n x A = 0	n x A = 0	n x A = 0		Axial symmetry	Axial symmetry	
Heat transfer	-n . q = 0	-n . q = 0	-n . q = 0	-n . q = 0	-n . q = 0	abs(ec.Jr*nr+ec.Jz*nz)*ϕ_a -0.4*σ_B*T^4	Axial symmetry	Axial symmetry	-0.4*σ_B*T^4 j_i*V_i - j_e*ϕ_c
Turbulant flow		Inlet, pressure with no viscous stress (p_{ent} = 0) [I_T=0.05, L_T=0.07*(2radc), U_{ref} = 1*f_u]	Oulet outflow (p_{ext} = 0)			Wall - Slip	Axial symmetry	Axial symmetry	Wall - Slip

n = surface normal vector; J = electric current density; V = voltage; A = Magnetic vector potential; q = heat flow; σ_B = Stefan-Boltzmann
ϕ_a = anode work function; ϕ_c = cathde work function; V_i = air ionization potential; j_i = ion current; j_e = electron current;
I_T = Turbulence intensity; L_T = Turbulent length scale; U_{ref} = Reference velocity scale.

Initial electric conductivity model

A 1-D model (also constructed in COMSOL Multiphysics) was developed to couple the electron transport partial differential equations and the electric current partial differential equations, to calculate the initial electric conductivity. This model is to avoid the temperature boundary condition at the cathode (3,500 K) that is assumed by many researchers [19-21] to resolve the issue of zero electric conductivity at room temperature. The model is represented in Figure 3 and its boundary conditions are listed in Table 1. Line 1-2 of the model represents the cathode region, while line 2-3 represents the air plasma region. The cross-sectional area of the 1-D model at node-1 equals the cathode inlet area and the cross-sectional area at node-2 equals the cathode surface area of the h-k-m region. The lightning strike electric current is applied at node-1 with Equation 29 [5],

$$I(t) = 11300\left(e^{-700 \bullet t} - e^{-2000 \bullet t}\right) \tag{29}$$

The electron cold-field emissions flux is applied at node-2. A fully coupled time-dependent analysis is simulated for a total of 4E-5 seconds. The air plasma electric conductivity is initially that of air at a temperature of 300 K (1e-14 S/m) (Kamsali et al. [31].). Then, the electric conductivity is calculated using equation (19) and averaged along line 2-3. The electric field reaches a value of 45,000 Townsend at 5E-7 seconds at the cathode surface, which triggers two actions simultaneously, electron cold-field emissions and ionization.

The electric field at the cathode surface was validated by running short-time simulations (1E-5 seconds) on the 2-D axisymmetric model that was discussed in the previous section. The average electric conductivity reaches a value of 8,232 S/m (N_e = 5.6E22 1/m_3) between t = 7E-7 and 3E-5 seconds (shown in Figure 4). Once the electric conductivity increases the electric field value drops, which stops electron-cold field emissions and the electron attachment process dominates. Thus, the average electric conductivity settles at a value of 0.6 S/m at 3.92E-5 seconds. It was found that extending the simulation time further does not significantly change the average electric conductivity. This extra electric conductivity opens a highly conducting path, and is applied in the 2-D MHD model near the cathode region as $\sigma = \sigma_{ext} \exp(-(E_m / E_h).(\mathrm{r}/ r_{cath}))$. Where, E_m and E_h are the electric field at m and h respectively on Figure 3. Thus, the extra electric conductivity is only near the cathode region. r_{cath} is the cathode radius at line a-b.

Table 1: 1-D model boundary conditions.

	1	2	3
Electrical current	-n . J = J_n	Change Cross-section = A_sur	V = 0
Electron Transport		-n . Ne = J_{FN}/e_{const}	Ne = 0
1-2 material properties is Tungsten [solid, Ho et al]. 2-3 material properties is air plasma. Air electric conductivity = 1e-14 S/m			

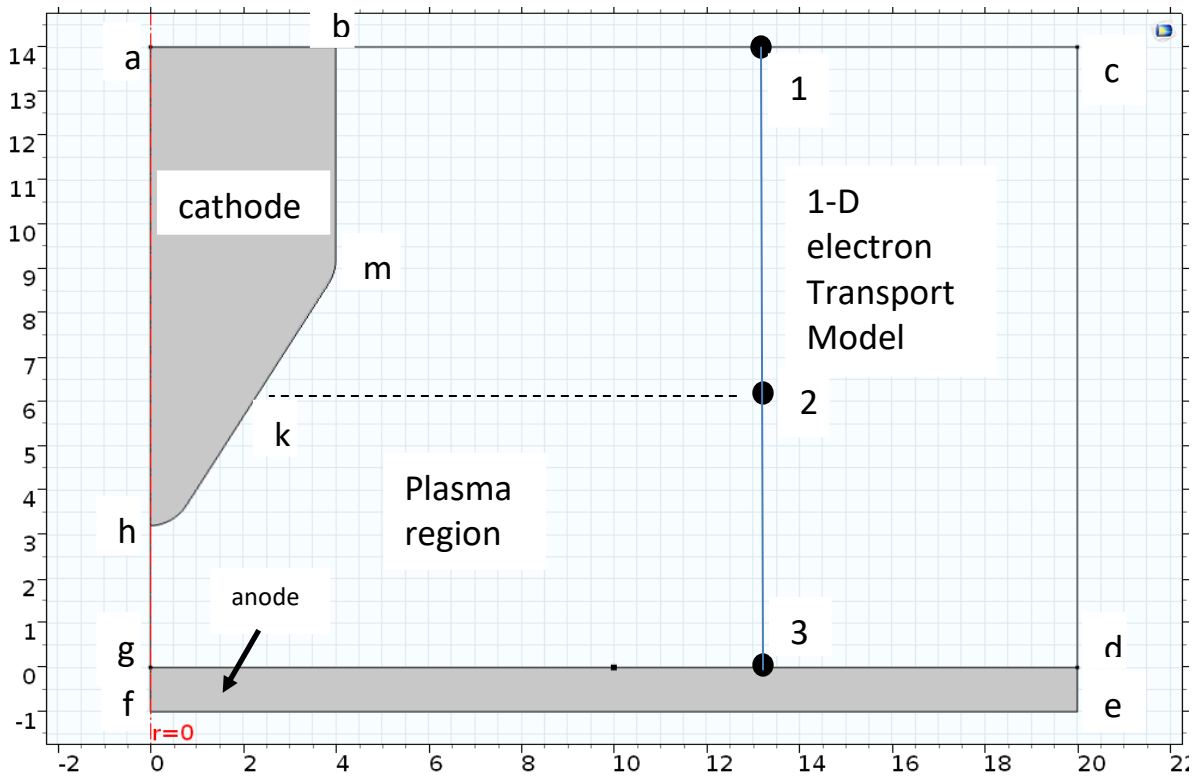

Figure 3: Axisymmetric and the 1-D Geometrical domain [mm].

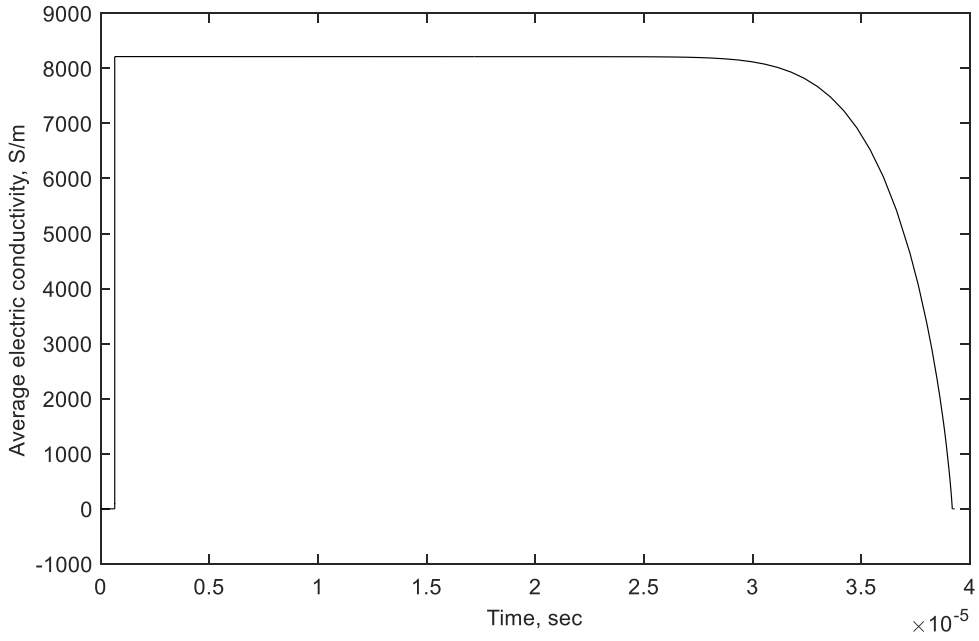

Figure 4: 1-D model average electric conductivity of plasma domain (2-3).

Results

Initially a laminar flow solution was examined but over a large range of mesh and boundary condition trials the simulations consistently suffered from convergence problems. Reasonable solutions were achievable up to approximately 90 milliseconds after which the plasma flow velocity vector near the cathode region was predicted to travel in a negative r-direction. This plasma flow direction confined the convection heat transfer in the region of the cathode, which led to an extremely high plasma temperature (> 80,000 K). The total simulation time of a waveform-B lightning strike event is 5 microseconds and the electric current reaches its maximum around 0.8 microseconds (Figure 1). Reaching such a high temperature after such a short duration is not representative and suggests a modelling deficiency. Further the flow Reynold's number was considered high (> 2E5) for a laminar flow solution to be accepted [41].

Conversely the turbulent flow simulation trials consistently produced plasma flow velocities which traveled in the positive r-direction. This led to convection heat transfer in the positive r-direction and maximum temperatures of the order of 40,000 K at approximately 0.8 microseconds. Figures 5 to 7 illustrate typical numerical results of temperature, velocity, and pressure at 1.0 millisecond for a turbulent flow simulation. Maximum-scaled values for the plasma pressure, velocity and temperature versus time are also presented in Figure 8. The temperature results demonstrates that despite the air plasma core temperature being in the range of 10,000 K the cathode and anode surface temperature is only in the range of 300 K. This is due to the short time duration of the lightning strike event and is validated by experimental results [37, 38, 39] in which the cathode surface is not evaporated. Moreover, in certain lightning strike test setups a rubber head is installed near the cathode to reduce the lightning strike channel expansion pressure effects and again the rubber head is not typically damaged by heat. This indicates that the main factor in causing damage at the anode surface for this test setup is the electric resistivity and not the heat flux from the air plasma.

A large-scale Windows cluster and a desktop Windows work-station were used to perform the final simulations and the initial simulation trials. The use of the desktop work-station illustrates the utility of the proposed modelling approach. The presented results were achieved in 237 hours using a single node (16 cores, 3 GHz) of the desktop workstation with 64 GB of RAM.

Discussion

A major unknown and question within the aerospace community to this point as been the question of which mechanism causes more damage to the structure, surface electric current or surface pressure? Thus, Figure 9 shows the electric current density and the pressure at the node and the cathode surfaces. The pressure at the anode and the cathode were scaled with respect to the pressure peak value at the cathode surface (0.161 MPa). The anode electric current density reaches its peak value early in the simulation as a channel is formed between the cathode and anode. This behaviour is efficiently captured within the simple 1-D coupled model (Figure 4). Once the plasma reaches the anode surface and due to air electric resistivity, the channel starts to heat up and expand. Expansion of the plasma channel leads to a wider anode surface area that is exposed to electric current and the average electric current density is reduced. Ultimately the Waveform-B electric current reaches its peak around 0.86 milliseconds. During the simulated

Waveform-B lightning strike (up to its peak), the anode surface pressure is only around 0.10 MPa, while the cathode surface pressure is around 0.12 MPa. Two points from this result are; the cathode surface pressure is marginally higher for this particular experimental setup in which the cathode and anode are only a few millimetres apart. For a waveform-B profile the anode surface pressure is far from a significant magnitude which could cause mechanical damage. Both these conclusions are new and illustrate the value of the proposed modelling approach.

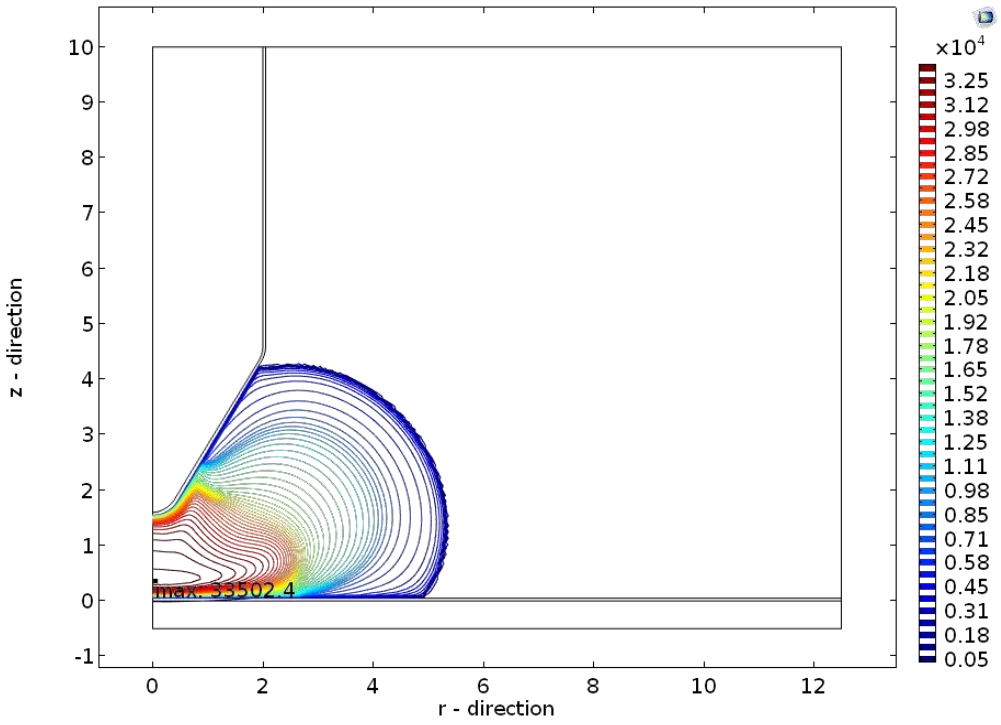

Figure 5: Temperature profile waveform-B at time = 1.0 millisecond.

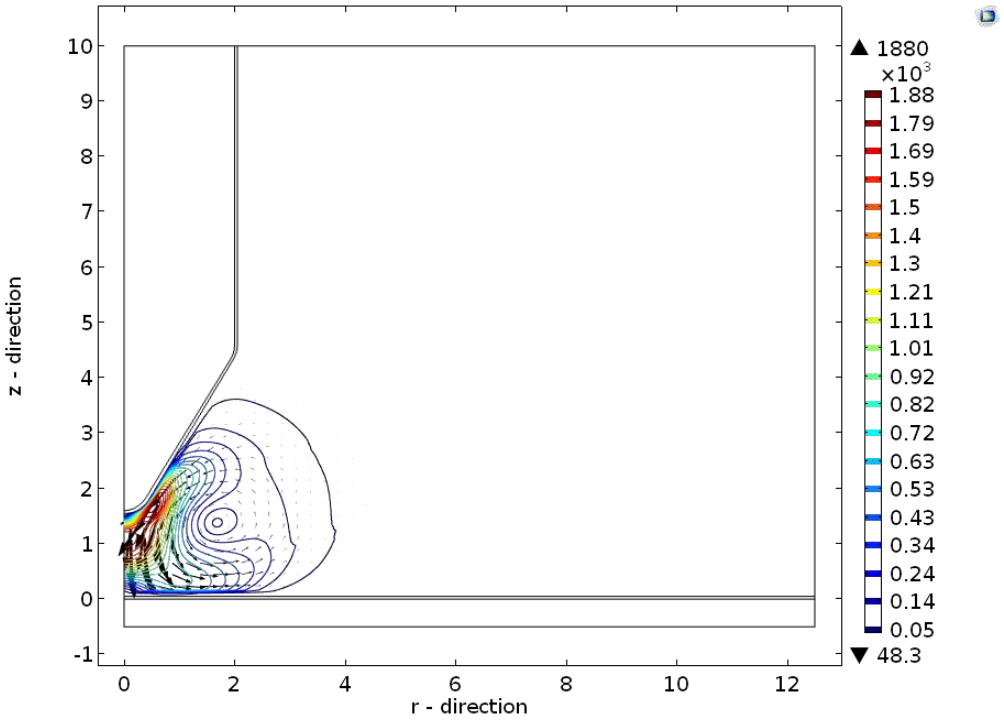

Figure 6: Velocity profile waveform-B at time = 1.0 millisecond.

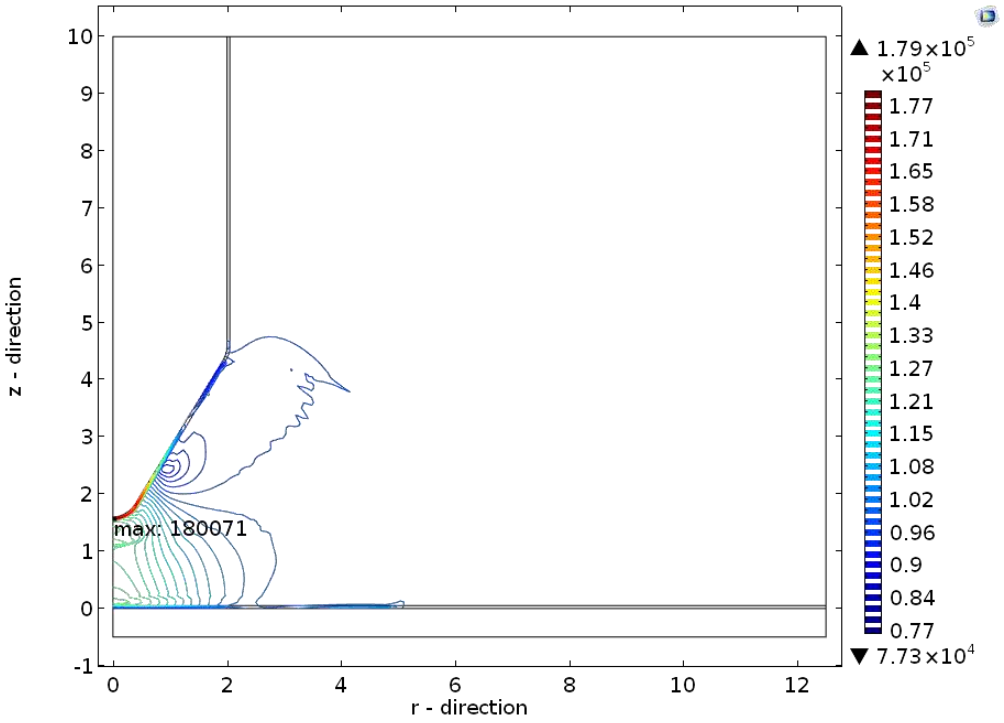

Figure 7: Absolute pressure profile waveform-B at time = 1.0 millisecond.

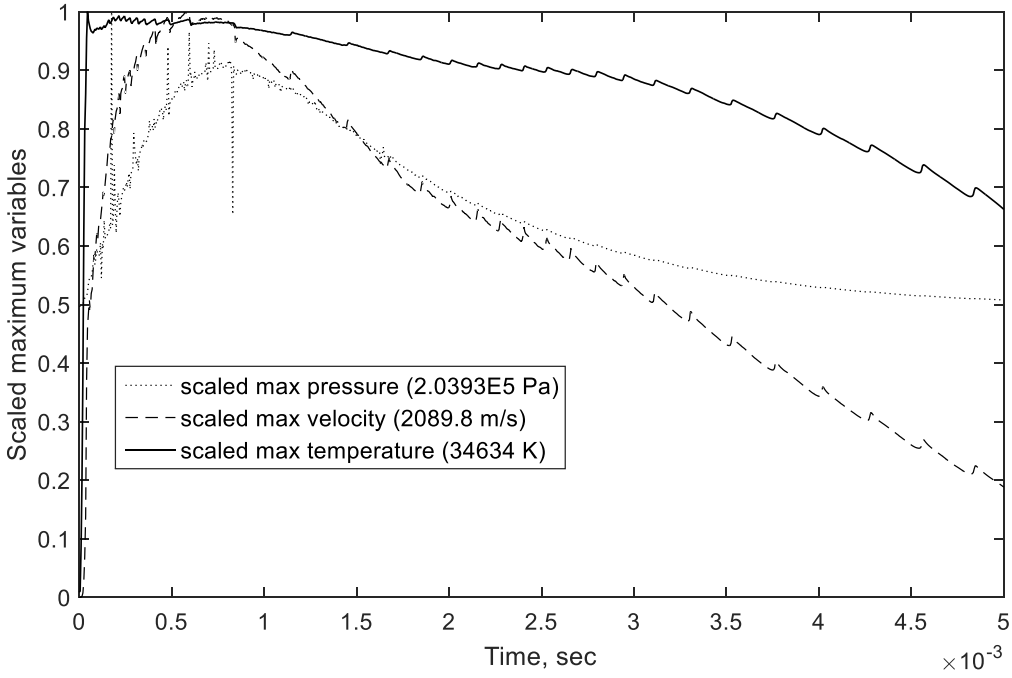

Figure 8: Waveform-B scaled maximum pressure, velocity, temperature.

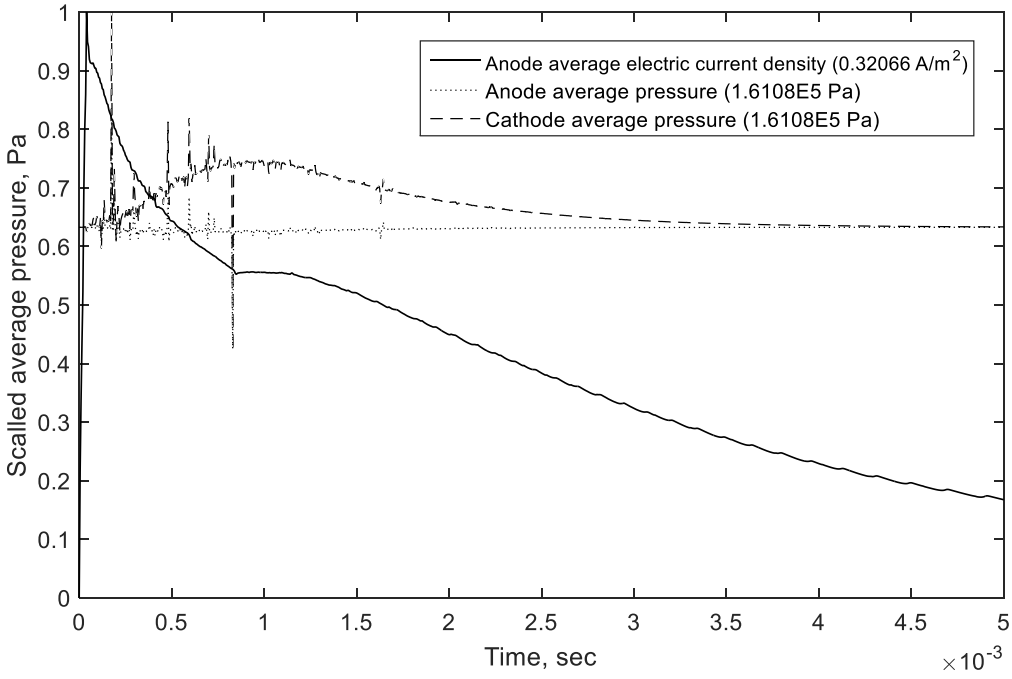

Figure 9: Waveform-B scaled surface electric current density and pressure.

Conclusion & future work

This paper presents an approach to use similitude theory along with MHD equations to create prototype models that can efficiently model the key physical behaviours, which occur during a lightning strike event. A prototype model has been developed based on a comprehensive electromagnetic model and appropriate similarity constraints. The approach has been demonstrated for a Waveform-B lightning strike event and is capable of estimating current flux, temperature, velocity, and pressure profiles efficiently in less than 10 days. A numerical approach is proposed and demonstrated to resolve the numerical difficulty of simulating the nearly zero electrical conductivity of air at room temperature. Simulations considering both laminar and turbulent flow have been considered, modelling a test configuration from literature designed to inspect composite material performance. The assumption of laminar flow during lightning strike led to infeasible results. Turbulent flow equations led to results that are considered feasible. Predicted peak temperatures (of the order of ~40,000 K) and pressures (of the order of 0.1-0.2 MPa) suggest that the pressure loading during a Waveform-B event will have a minimal effect on composite material damage.

Further investigation is require to assess the ability of the proposed approach to model Waveform-A & -D. In addition, it would be prudent to investigate the use of a Finite Volume method, which may outperform the Finite Element based approach particularly in achieving flow and pressure predictions. Pushing the code further to calculate air plasma chemical composition for more accurate transport properties and possible plasma-surface interaction investigation is in progress.

References

1. G. Abdelal, A. Murphy. Nonlinear numerical modelling of lightning strike effect on composite panels with temperature dependent material properties. Composite Structures, Vol. 109, pp. 268-278, 2014.
2. Jiajing Pan, Shengsun Hu, Lijun Yang, Shujun Chen, Numerical analysis of the heat transfer and material flow during keyhole plasma arc welding using a fully coupled tungsten–plasma–anode model, Acta Materialia, Volume 118, 1 October 2016, Pages 221-229.
3. M Boulos, P Fauchais, E Pfender. Thermal Plasmas, Fundamentals and Applications – Vol. 1, Springer, 1994
4. Documentation for COMSOL, Release 4.4, COMSOL Inc., USA.
5. Ever Barbero. Multifuncional Composites, CreateSpace Independent Publishing, 2015.
6. L. Chemartin, P. Lalande, B. Peyrou, A. Chazottes, P.Q. Elias, C. Delalondre, B.G. Cheron, F. Lago. Direct Effects of Lightning on Aircraft Structure: Analysis of the Thermal, Electrical and Mechanical Constraints. Aerospace Lab, December 2012, pp. 1-15.
7. G. Abdelal, A. Murphy. Multiphysics Simulation of Thermal Plasma Produced by Lightning Strike on Aircraft Structures. Paper presented at 4th Aircraft Structural Design Conference, Belfast, United Kingdom, 7-9 Oct 2014.
8. Kulsrud, R. M., Sagdeev, R. N., Rosenbluth, M. N., MHD description of plasma: Handbook of plasma physics. Oct 1980; 66 p; PPPL--1705; Available from NTIS., PC A04/MF A01.

9. Alfvén, H., Existence of electromagnetic-hydrodynamic waves, 1942, Nature, Vol. 150, pp. 405
10. Alfvén, H., On the cosmogony of the solar system III", Stockholms Observatoriums Annaler, vol. 14, pp.9.1-9.29.
11. L. Kalikhman. Elements of Magnetogasdynamics. Saunders, London, 1967.
12. Barbu, V. et al., Exact controllability magneto-hydrodynamic equations, 2003, Communications on Pure and Applied Mathematics 56: pp. 732–783.
13. Biskamp, Dieter. Nonlinear Magnetohydrodynamics. Cambridge, England: Cambridge University Press, 1993. 378 p. ISBN 0-521-59918-0.
14. Davidson, Peter Alan, An Introduction to Magnetohydrodynamics, 2001, Cambridge University Press, Cambridge, England, ISBN 0-521-79487-0.
15. Pai, Shih-I, Magnetogasdynamics and Plasma Dynamics, 1962, Springer-Verlag, Vienna, ISBN 0-387-80608-3.
16. Popa, C. and Sritharan, S. S., Fluid-magnetic splitting methods for magneto-hydrodynamics, 2003, Mathematical Methods and Models in Applied Sciences 13(6): pp. 893–917.
17. Roberts, Paul H., An Introduction to Magnetohydrodynamics, 1976, Longmans Green, London, OCLC 489632043
18. H.G. Fan, Y.W. Shi, Numerical simulation of the arc pressure in gas tungsten arc welding, J. Mater. Process. Tech. 61 (1995) 302–308.
19. C.S. Wu, J.Q. Gao, Analysis of the heat flux distribution at the anode of a TIG welding arc, Comput. Mater. Sci. 24 (2001) 323–327.
20. H.G. Fan, Y.W. Shi, S.J. Na, Numerical analysis of the arc in pulsed current gas tungsten arc welding using boundary-fitted coordinate, J. Mater. Process. Tech. 72 (1997) 437–445.
21. F. Lu, X. Tang, H. Yu, S. Yao, Modeling and finite element analysis on GTAW arc and weld pool, Comput. Mater. Sci. 29 (2003) 371–378.
22. F. Lago, J.J. Gonzalez, P. Freton, A. Gleizes, A numerical modelling of an electric arc and its interaction with the anode: Part I. The two-dimensional model, J. Phys. D: Appl. Phys. 37 (2004) 883–897.
23. J.J. Gonzalez, F. Lago, P. Freton, M. Masquére, X. Franceries, A numerical modelling of an electric arc and its interaction with the anode: Part II. The three-dimensional model- influence of external forces on the arc column, J. Phys. D: Appl. Phys. 38 (2005) 306–318.
24. F. Lu, X. Tang, H. Yu, S. Yao, Numerical simulation on interaction between TIG welding arc and weld pool, Comput. Mater. Sci. 35 (2006) 458–465.
25. M. Tanaka, H. Terasaki, M. Ushio, J.J. Lowke, A unified numerical modelling of stationary tungsten-inert-gas welding process, Metall. Mater. Trans. A 33 (7) (2002) 2043–2052.
26. M. Tanaka, J.J. Lowke, Predictions of weld pool profiles using plasma physics, J. Phys. D: Appl. Phys. 40 (2007) R1–R23.
27. L. Sansonnens, M. Ushio, J.J. Lowke, Prediction of properties of free burning arcs including effects of ambipolar diffusion, J. Phys. D: Appl. Phys. 33 (2000) 148–157.
28. J.J. Lowke, R. Morrow, J. Haidar, A simplified unified theory of arcs and their electrodes, J. Phys. D: Appl. Phys. 30 (1997) 2033–2042.
29. M. Tanaka, H. Terasaki, M. Ushio, J.J. Lowke, A unified numerical modelling of stationary tungsten-inert-gas welding process, Metall. Mater. Trans. A 33 (7) (2002) 2043–2052.

30. A Traidia, F Roger. Numerical and experimental study of arc and weld pool behaviour for pulsed current GTA welding. International Journal of Heat and Mass Transfer, 54, 2011 2163–2179.
31. Nagaraja Kamsali, B.S.N. Prasad and Jayati Datta . The Electrical Conductivity as an Index of Air Pollution in the Atmosphere, Advanced Air Pollution, Dr. Farhad Nejadkoorki (Ed.), ISBN: 978-953-307-511-2, InTech (2011), DOI: 10.5772/17163.
32. Fowler, R. H. & Nordheim, L. W. 1928 Electron emission in intense electric fields. Proc. R. Soc. A 119, 173–181.
33. Richard G. Forbes and Jonathan H. B. Deane. Reformulation of the standard theory of Fowler–Nordheim tunnelling and cold field electron emission. Proc. R. Soc. A (2007) 463, 2907–2927.
34. Geroge S., Theory of Models of Electromagnetic Systems. Proceedings of the IRE, 36, 1948, 1364-1370.
35. L. E. Kalikhman (1967). *Elements of Magnetogasdynamics*. W. B. Saunders Company.
36. Victor J. Skoglund (1976). Similitude: Theory and applications. International textbook company.
37. Yoshiyasu Hirano, Shingo Katsumata, Yutaka Iwahori, Akira Todoroki. Artificial lightning testing on graphite/epoxy composite laminate. Composites: Part A 41 (2010) 1461–1470.
38. Toshio Ogasawara, Yoshiyasu Hirano, Akinori Yoshimura. Coupled thermal–electrical analysis for carbon fiber/epoxy composites exposed to simulated lightning current. Composites: Part A 41 (2010) 973–981.
39. Paolo Feraboli, Mark Miller. Damage resistance and tolerance of carbon/epoxy composite coupons subjected to simulated lightning strike. Composites: Part A 40 (2009) 954–967.
40. M. Capitelli, G. Colonna, C. Gorse, and A. D'Angola. Transport properties of high temperature air in local thermodynamic equilibrium. Eur. Phys. J. D **11**, (2000) 279-289.
41. Faith A., An Introduction to Fluid Mechanics. Cambridge University Press, 2013.